




## Article

# A p-Tyr42 RhoA Inhibitor Promotes the Regeneration of Human Corneal Endothelial Cells by Ameliorating Cellular Senescence

Hyeon Jung Kim <sup>1,2,†</sup>, Jin Sun Hwang <sup>1,2,†</sup>, Kyung Bo Noh <sup>1,2,†</sup>, Sun-Hee Oh <sup>1,2</sup>, Jae-Bong Park <sup>3</sup> and Young Joo Shin <sup>1,2,\*</sup> 

<sup>1</sup> Department of Ophthalmology, Hallym University Medical Center, Hallym University College of Medicine, Seoul 07442, Republic of Korea; kylehoh@outlook.kr (K.B.N.); sunny5@hallym.ac.kr (S.-H.O.)

<sup>2</sup> Hallym BioEyeTech Research Center, Hallym University College of Medicine, Seoul 07442, Republic of Korea

<sup>3</sup> Department of Biochemistry, Hallym University College of Medicine, Chuncheon 24252, Republic of Korea

\* Correspondence: schinn@hallym.or.kr; Tel.: +82-2-6960-1240

† These authors contributed equally to this work.

**Abstract:** The development of treatment strategies for human corneal endothelial cells (hCECs) disease is necessary because hCECs do not regenerate in vivo due to the properties that are similar to senescence. This study is performed to investigate the role of a p-Tyr42 RhoA inhibitor (MH4, ELMED Inc., Chuncheon) in transforming growth factor-beta (TGF- $\beta$ )- or H<sub>2</sub>O<sub>2</sub>-induced cellular senescence of hCECs. Cultured hCECs were treated with MH4. The cell shape, proliferation rate, and cell cycle phases were analyzed. Moreover, cell adhesion assays and immunofluorescence staining for F-actin, Ki-67, and E-cadherin were performed. Additionally, the cells were treated with TGF- $\beta$  or H<sub>2</sub>O<sub>2</sub> to induce senescence, and mitochondrial oxidative reactive oxygen species (ROS) levels, mitochondrial membrane potential, and NF- $\kappa$ B translocation were evaluated. LC3II/LC3I levels were determined using Western blotting to analyze autophagy. MH4 promotes hCEC proliferation, shifts the cell cycle, attenuates actin distribution, and increases E-cadherin expression. TGF- $\beta$  and H<sub>2</sub>O<sub>2</sub> induce senescence by increasing mitochondrial ROS levels and NF- $\kappa$ B translocation into the nucleus; however, this effect is attenuated by MH4. Moreover, TGF- $\beta$  and H<sub>2</sub>O<sub>2</sub> decrease the mitochondrial membrane potential and induce autophagy, while MH4 reverses these effects. In conclusion, MH4, a p-Tyr42 RhoA inhibitor, promotes the regeneration of hCECs and protects hCECs against TGF- $\beta$ - and H<sub>2</sub>O<sub>2</sub>-induced senescence via the ROS/NF- $\kappa$ B/mitochondrial pathway.

**Keywords:** RhoA; human corneal endothelial cells; cell death; proliferation; TGF- $\beta$ ; oxidative stress



**Citation:** Kim, H.J.; Hwang, J.S.; Noh, K.B.; Oh, S.-H.; Park, J.-B.; Shin, Y.J. A p-Tyr42 RhoA Inhibitor Promotes the Regeneration of Human Corneal Endothelial Cells by Ameliorating Cellular Senescence. *Antioxidants* **2023**, *12*, 1186. <https://doi.org/10.3390/antiox12061186>

Academic Editor: Marc Kantorow

Received: 14 April 2023

Revised: 18 May 2023

Accepted: 27 May 2023

Published: 30 May 2023



**Copyright:** © 2023 by the authors. Licensee MDPI, Basel, Switzerland. This article is an open access article distributed under the terms and conditions of the Creative Commons Attribution (CC BY) license (<https://creativecommons.org/licenses/by/4.0/>).

## 1. Introduction

Human corneal endothelial cells (hCECs) are located on the innermost surface of the cornea and participate in the dehydration of the corneal stroma. They reportedly have limited proliferative capacity in vivo, although supplementation with various growth factors causes them to proliferate in vitro. Thus, efforts have been made to proliferate hCECs in vivo [1,2]. Rho-associated coiled-coil-containing protein kinase (ROCK) inhibitors promote the proliferation of corneal endothelial cells (CECs), although they inhibit proliferation of other cell types [3,4]. This is because ROCK inhibitors inhibit senescence [5,6]. Corneal endothelial cells (CECs) are different from vascular endothelial cells. CECs have a flattened hexagonal shape [7], while vascular endothelial cells have a spindle-like shape [8]. CECs are also found only in the cornea [7], while vascular endothelial cells are found throughout the body [9]. CECs do not express VE-cadherin, which has been known to be expressed in vascular endothelial cells [9]. CECs has been previously reported to express E-cadherin [10].

Transforming growth factor-beta (TGF- $\beta$ ) is a major cytokine that induces senescence [11], the process in which ROCK plays an important role [12]. Rho/ROCK signaling mediates TGF- $\beta$ -induced actin organization and fibrosis via nuclear factor kappa-light-chain-enhancer of activated B cells (NF- $\kappa$ B) [13–15], where ROCK2 is particularly

involved [15]. Moreover, TGF- $\beta$  suppresses the proliferation of rabbit CECs in vitro [16], and inhibition of TGF- $\beta$  signaling enables hCEC expansion in vitro for use in regenerative medicine [17], although it promotes cell barrier function upon maturation of CECs [18]. Furthermore, TGF- $\beta$  receptor inhibitors suppress endothelial–mesenchymal transformation of hCECs [19]. TGF- $\beta$  induces CEC senescence by increasing mitochondrial reactive oxygen species (ROS) levels [20]. Additionally, activation of TGF- $\beta$  induces cell death via the unfolded protein response pathway in Fuchs’ endothelial corneal dystrophy [21].

The Rho/ROCK pathway is an important signaling pathway critically involved in cell proliferation, differentiation, migration, and apoptosis [22]. Rho is a member of the Rho subfamily of GTPases and includes RhoA, B, C, D, and E [23]. Rho proteins are regulated by various factors that control their activity and function within cells [23]. For example, guanine nucleotide exchange factor (GEF) leads to the release of GDP and binding of GTP to Rho proteins [24], causing their activation. GEFs are activated by several types of cell surface receptors including receptor tyrosine kinases, G-protein-coupled receptors, cytokines, and integrins [25]. ROCK is one of the most crucial downstream effectors of Rho [26] and belongs to the serine/threonine protein kinase family [26]. ROCK has two highly homologous isomers: ROCK1 and ROCK2 [27]. ROCK substrates vary depending on the tissue type [26]. ROCK1 is abundantly expressed in immunological cells, whereas ROCK2 is expressed in the brain and heart [28,29]. The function of ROCK1 and ROCK2 in modulating stress-induced actin dynamics, cell migration, and detachment is different [30], in that ROCK1 is involved in destabilizing actin cytoskeleton, whereas ROCK2 is involved in stabilizing actin cytoskeleton [30]. ROCK2 mediates cardiac hypertrophic responses [31,32], while ROCK1 participates in cardiac fibrosis [33]. ROCK1 is mainly activated by RhoA in its GTP-bound form, while ROCK2 is preferentially activated by p-Tyr42 RhoA in addition to the GTP-bound form [34]. In this study, we used a p-Tyr42 RhoA inhibitor as an inhibitor of the Rho/ROCK signaling pathway to induce the regeneration of hCECs. p-Tyr42 RhoA GTPase promotes reactive oxygen species (ROS) production via the phosphorylation of p47phox by ROCK and activates NF- $\kappa$ B [35,36].

ROCK2 is suspected to have a greater role in the proliferation of CECs and selective inhibition of ROCK2 via the inhibition of the p-Tyr42 RhoA pathway; the upstream signaling pathway of ROCK2 is expected to be the main mechanism of CEC proliferation and senescence. Thus, in this study, we investigated the role of a p-Tyr42 RhoA inhibitor in TGF- $\beta$ -induced cellular senescence of hCECs.

## 2. Materials and Methods

### 2.1. Cell Culture

This study was performed in accordance with the tenets of the Declaration of Helsinki and reviewed and approved by the institutional review board/ethics committee of the Hallym University Medical Center. Human corneas were purchased from Eversight Eye Bank (Ann Arbor, MI, USA) and hCECs were cultured as previously described [37].

Cultured hCECs were treated with the p-Tyr42 RhoA inhibitor MH4 (10  $\mu$ M; ELMED Inc., Chuncheon, Korea), TGF- $\beta$  (10 ng/mL; ab50036, Abcam, Cambridge, MA, USA), or H<sub>2</sub>O<sub>2</sub> (2 mM) in 5% CO<sub>2</sub> incubator for 48 h. The hCECs were harvested for subsequent experiments.

### 2.2. Cell Viability and Proliferation Assays

Cell counting kit-8 (CCK-8; Dojindo, Kumamoto, Japan) was used to assess cell viability. Briefly, cells ( $1 \times 10^4$ ) were cultured in 96-well plates and treated with the CCK-8 reagents for 2 h. The cell viability was evaluated by measuring the optical density at 450 nm using a microplate reader (Synergy HTX, BioTek, Winooski, VT, USA) [38].

Bromodeoxyuridine (BrdU) proliferation assay kit (Roche Diagnostics, GmbH, Mannheim, Germany) was used to evaluate the cell proliferation rate according to the manufacturer’s protocol. Cells ( $5 \times 10^3$  cells/well) were placed in 96-well plates and incorporated with BrdU at 37 °C and 5% CO<sub>2</sub>. After incubating the cells with FixDenat solution for 30 min at 25 °C, the cells were treated with anti-BrdU-POD reagents for 90 min at 25 °C. The substrate

reagents were put into each well, and incubated for 15 min at 25 °C. Then, 1 M H<sub>2</sub>SO<sub>4</sub> solution was put into each well. Absorbance was evaluated at 450 nm using a microplate reader (Synergy HTX, BioTek) [39]. Proliferation rates are determined as the fold of controls.

Cytotoxicity was assessed using a lactate dehydrogenase (LDH) cytotoxicity detection assay (MK401, Takara Bio Inc., Shiga, Japan). Briefly, cell culture supernatants containing LDH released from damaged cells were obtained, added to 96-well plates, and incubated for 10–30 min with the reaction mix. Absorbance was assessed at 490 nm using a multi-mode microplate reader (Synergy HTX, BioTek) [40].

To construct a growth curve, cells were incubated under controlled conditions. At regular intervals, the number of cells is determined by counting using a microscope at three low-power fields ( $\times 5$ ).

### 2.3. Cell Cycle Analysis

Cell cycle was analyzed using flow cytometry (CytoFLEX, Beckman Coulter Life Sciences, Miami, FL, USA) and propidium iodide (PI) reagent. The number of cells in each phase was compared.

### 2.4. Cell Adhesion Assay

Cell adhesion was evaluated for 2 or 6 h. Confluent cultured cells were pretreated with 10  $\mu$ M MH4 for 30 min. The cells were trypsinized, resuspended in the corresponding culture medium, and standardizing to an equal cell number of  $2 \times 10^5$ /mL. The equal number of cells (50  $\mu$ L) was put into each well of 96-well plates. Cells were allowed to adhere to the bottom of plates for 2 or 6 h, and non-adherent cells were rinsed off with PBS. Then, 4% paraformaldehyde was used for the fixation of cells for 30 min at 25 °C and stained with 0.1% crystal violet solution for 1 h. The culture dishes were extensively rinsed with distilled water to draw off excess dye, and the stain was dissolved with 10% acetic acid. Optical density at 570 nm was determined using a multi-mode spectrophotometer.

### 2.5. Immunofluorescence Staining

hCECs were cultured on cell culture slides (SPL Life Sciences, Seoul, Korea), washed with PBS, and fixed using 4% paraformaldehyde for 30 min. Permeabilization was performed for 10 min using 0.5% Triton X-100 and blocking was performed for 60 min using 1% skim milk at 25 °C. Then, the cells were treated with mouse anti-human Ki-67 antibody (sc-23900; Santa Cruz Biotechnology, Santa Cruz, CA, USA), mouse anti-human E-cadherin antibody (sc-8426; Santa Cruz Biotechnology), or rabbit anti-human NF- $\kappa$ B antibody (sc-372; Santa Cruz Biotechnology) at 4 °C, followed by rinsed with PBS. The cells were treated with either fluorescein isothiocyanate-conjugated goat anti-rabbit IgG antibody (1:100) for 2 h at 25 °C and the nucleus were stained with Hoechst 33342 reagent (1:2000; Molecular Probes, Eugene, OR, USA). The cells were evaluated under a fluorescence microscope (DMi8, Leica Microsystems, Hesse, Germany) and photographs were captured.

hCEC adhesion was assessed using the actin staining marker phalloidin. F-actin was stained using Alexa Fluor 488H phalloidin (Molecular Probes) and Hoechst 33342 nuclear stain, and cells were evaluated under a fluorescence microscope (DMi8; Leica Microsystems).

### 2.6. Western Blotting

Radioimmunoprecipitation assay buffer (Biosesang, Seoul, Korea) including phosphatase (PhosSTOP; Roche, Basel, Switzerland) inhibitor cocktails and protease (Sigma-Aldrich, St. Louis, MO, USA) was employed to obtain total proteins. Western blot was conducted by standard methods. Briefly, 5% skim milk was added for 1 h to block nonspecific binding. The primary antibodies used were: mouse anti-ROCK1 antibody (sc-17794, Santa Cruz Biotechnology, 1:500 dilution), mouse anti-ROCK2 antibody (sc-398519, Santa Cruz Biotechnology, 1:500 dilution), mouse anti-LC3 antibody (M186-3, MBL, Fujioka-Shi, 1:1000 dilution), and rabbit anti-GAPDH antibody (LF-PA0212, Abfrontier, Seoul, 1:5000 dilution). A horseradish peroxidase-conjugated secondary antibody and WEST-Queen™

Western Blot Detection Kit (iNtRON Biotechnology, Seongnam, Korea) were employed. Video image analysis was used to quantify the immunoreactive band.

To evaluate NF- $\kappa$ B levels in nucleus and cytoplasm, NE-PER nuclear and cytoplasmic extraction reagents (Thermo Fisher Scientific Inc., Waltham, MA, USA) was used. Cells were harvested, rinsed with PBS, and centrifuged at  $200\times g$  for 5 min. After nuclear proteins were extracted, cytoplasmic extraction reagent I including phosphatase and protease inhibitor cocktails (1:100) was put into the samples for 10 min on ice. Cytoplasmic extraction reagent II was put into the samples for 1 min. Samples were centrifuged at  $16,000\times g$  for 5 min at 4 °C. Then, Western blotting was performed. Primary antibodies were as follows: rabbit anti-human NF- $\kappa$ B antibody (sc-372; Santa Cruz Biotechnology),  $\beta$ -actin (LF-PA0207, Abfrontier, Seoul, 1:5000 dilution) and rabbit anti-GAPDH antibody (LF-PA0212, Abfrontier, Seoul, 1:5000 dilution).

### 2.7. Senescence- $\beta$ -Galactosidase Assay and Cell Size Measurements

Senescence- $\beta$ -galactosidase staining kit (BioVision) was used for senescence- $\beta$ -galactosidase (SA- $\beta$ -gal) staining. Briefly, after eliminating the growth medium, cells were washed with PBS. Each well was incubated with a fixative solution for 10–15 min at RT to fix the cells. After rinsing the cells with PBS, they were treated with  $\beta$ -galactosidase staining reagent at 37 °C overnight in a dry incubator.

To quantify the changes of cell shape, AxioVision Rel. 4.7 software (Carl Zeiss Meditec, Oberkochen, Germany) was used to outline the boundaries of cells and to measure the area of each cell in pixels. The measured areas were then represented as fold change, which is a measure of the relative difference between two values.

### 2.8. Mitochondrial Oxidative Stress Evaluation

MitoSOX<sup>TM</sup> Red (Invitrogen) was used according to the manufacturer's protocol to measure mitochondrial superoxide production. Cells were treated with 5  $\mu$ M MitoSOX<sup>TM</sup> solution for 20 min at 37 °C in the dark. Cytoflex analyzer (Beckman Coulter Life Sciences) was used to measure the fluorescence intensity at an excitation wavelength of 510 nm and emission wavelength of 590 nm.

### 2.9. Mitochondrial Membrane Potential Assay

Mitochondrial membrane potential was assessed using Muse<sup>TM</sup> MitoPotential assay kit (Merck Millipore, Guyancourt, France). The MitoPotential dye was employed to indicate the mitochondrial membrane potential, and 7-AAD was used to indicate cell death. Cytoflex flow cytometer (Beckman-Coulter, Brea, CA, USA) was used to analyze the data. JC-1 at a final concentration of 2.5  $\mu$ M was used for fluorescence microscopy to determine the mitochondrial membrane potential.

### 2.10. Real-Time Reverse Transcription-Polymerase Chain Reaction (qRT-PCR)

RNA was extracted from the cultured hCEnCs separately using the ReliaPrep<sup>TM</sup> RNA Miniprep Systems (Promega, Madison, WI, USA) [41]. First-strand cDNA was synthesized from 200 ng of oligonucleotide primers using a commercially available kit (GoScript Reverse Transcription System; Promega). Real-time quantification of transcripts was performed on a LightCycler<sup>®</sup> 96 (Roche Life Science, Mannheim, Germany) using the AccuPower 2X GreenStar qPCR Master Mix (Bioneer). The data were expressed as fold-changes relative to the control. The comparative CT or  $\Delta\Delta$ CT methods was used to conduct relative quantification. After normalization of the target gene to the reference gene,  $\beta$ -actin, the expression level of the target gene was presented as the relative change from the control treatment. The primers are described in Supplementary Table S1.

### 2.11. Transcriptome Analysis

Transcriptome was analyzed in order to investigate the effect of MH4 on gene expression patterns, regulatory mechanisms, and functional pathways within a biological system. RNA was extracted from cells treated with or without MH4. RNA sequencing was



conducted by MacroGen Inc. (Seoul, Republic of Korea, [www.macrogen.com](http://www.macrogen.com), accessed on 18 December 2022). Quant-IT RiboGreen (Invitrogen, #R11490) was used to measure total RNA amount. The samples are run on the TapeStation RNA screentape (Agilent, #5067-5576) for evaluation of the integrity of the total RNA. Only high-quality RNA preparations, with RIN greater than 7.0, were employed for RNA library construction.

Illumina TruSeq Stranded mRNA Sample Prep Kit (Illumina, Inc., San Diego, CA, USA, #RS-122-2101) was used to prepare a library with 1 ug of total RNA independently. Purification of the poly-A-containing mRNA molecules was performed using poly-T-attached magnetic beads. Then, the mRNA was fragmented into small pieces using divalent cations under elevated temperature. SuperScript II reverse transcriptase (Invitrogen, #18064014) and random primers was used to copy the cleaved RNA fragments into first-strand cDNA. Then, second-strand cDNA synthesis using DNA polymerase I, RNase H, and dUTP was conducted. The cDNA fragments went through an end repair process, the addition of a single 'A' base, and ligation of the adapters. The products were purged and enriched with PCR to create the final cDNA library. KAPA library quantification kits for Illumina Sequencing platforms according to the qPCR quantification protocol guide (KAPA BIOSYSTEMS, #KK4854) was used to quantify the libraries. TapeStation D1000 ScreenTape (Agilent Technologies, # 5067-5582) was used to qualify the libraries. The paired-end (2 × 100 bp) sequencing was performed by an Illumina NovaSeq (Illumina, Inc., San Diego, CA, USA).

FastQC v 0.11.7 (<http://www.bioinformatics.babraham.ac.uk/projects/fastqc/>, accessed on 11 September 2022) was used to evaluate quality control test of RNA-seq [42]. To eliminate 3' end adaptors and low-quality bases, Trimmomatic 0.38 (<http://www.usadellab.org/cms/?page=trimmomatic>, accessed on 11 September 2022) was used [43]. They were trimmed and then cleaned reads were aligned to the human reference genome (hg19) acquired from the University of California Santa Cruz genome browser by HISAT2 version 2.1.0 software (<https://ccb.jhu.edu/software/hisat2/index.shtml>, accessed on 11 September 2022) [44].

#### 2.12. Analysis of Differentially Expressed Genes (DEGs) and Functional Analyses of DEGs

To calculate transcript abundances and affirm differentially expressed genes (DEGs) between treated and control groups, StringTie version 1.3.4d (<https://ccb.jhu.edu/software/stringtie/>, accessed on 14 September 2022) and DESeq2 software were employed [45,46]. Transcript abundance was computed by fragments per kilobase of transcripts per million mapped reads (FPKM). DEGs were determined as genes satisfying the fold change (FC)  $\geq 2$  and a raw  $p$ -value  $< 0.05$  between groups. False discovery rate (FDR) control was performed by adjusting  $p$ -value calculated from Benjamini–Hochberg algorithm.

DEGs were aligned into the Gene Ontology (GO) databases to investigate the biological functions of DEGs. The  $q$ -value  $\leq 0.05$  calculated after the  $p$ -value was adjusted by multiple  $t$ -tests was employed as the threshold, and the GO term and path that were significantly enriched in the DEGs were investigated. GO enrichment analysis was conducted to classify DEGs based on specific biological functions using a ToppGene (<https://toppgene.cchmc.org/enrichment.jsp>, accessed on 18 May 2023) [47]. Molecular function of GO categories from ToppGene was presented. GO terms and pathways satisfying adjusted  $p$ -value  $< 0.05$  were considered significantly enriched.

#### 2.13. Autophagy Detection Imaging

CYTO-ID<sup>®</sup> Autophagy detection kit (ENZO) was used to monitor autophagy in live cells by fluorescent microscopy [48]. Briefly, cells were rinsed with PBS and incubated in Cyto-ID staining solution at 37 °C for 30 min in the dark. Cells were rinsed twice with PBS to eliminate the free dyes. Hoechst 33342 nuclear staining was performed, and cells were observed under a fluorescence microscope (DMi8; Leica Microsystems).

#### 2.14. Statistical Analysis

Data were presented as mean  $\pm$  standard deviation. GraphPad Prism v.9 (GraphPad Software, San Diego, CA, USA) was used for statistical analysis. An independent  $t$ -test

was used to compare two groups. One-way analysis of variance (ANOVA) followed by Tukey's multiple comparison test was used for more than two groups. All experiments were repeated more than three times. The individual values are presented in Figures, which show the number of repeats. The number of samples was decided using a two-sided test with  $\alpha = 0.05$  and  $\beta = 0.2$  (80% power).

### 3. Results

#### 3.1. MH4 Increases the Viability and Proliferation of Cultured hCECs

To evaluate the effect of MH4 on the health and function of cells, cell viability and proliferation rate were assessed. Cell viability is elevated and cytotoxicity is reduced by MH4 (Figure 1A,B). Moreover, MH4 elevates the cell proliferation rate (Figure 1C,D) and shifts the cells to the S phase (Figure 1E). The cells are small and less slender (Figure 1F). Immunofluorescence staining for Ki-67, a proliferation marker, shows that MH4 increases the number of Ki-67-positive cells (Figure 1G,H). Similarly, cell adhesion is increased by MH4 (Figure 1I,J). F-actin expression is decreased and E-cadherin expression is increased by MH4 (Figure 1K–N).

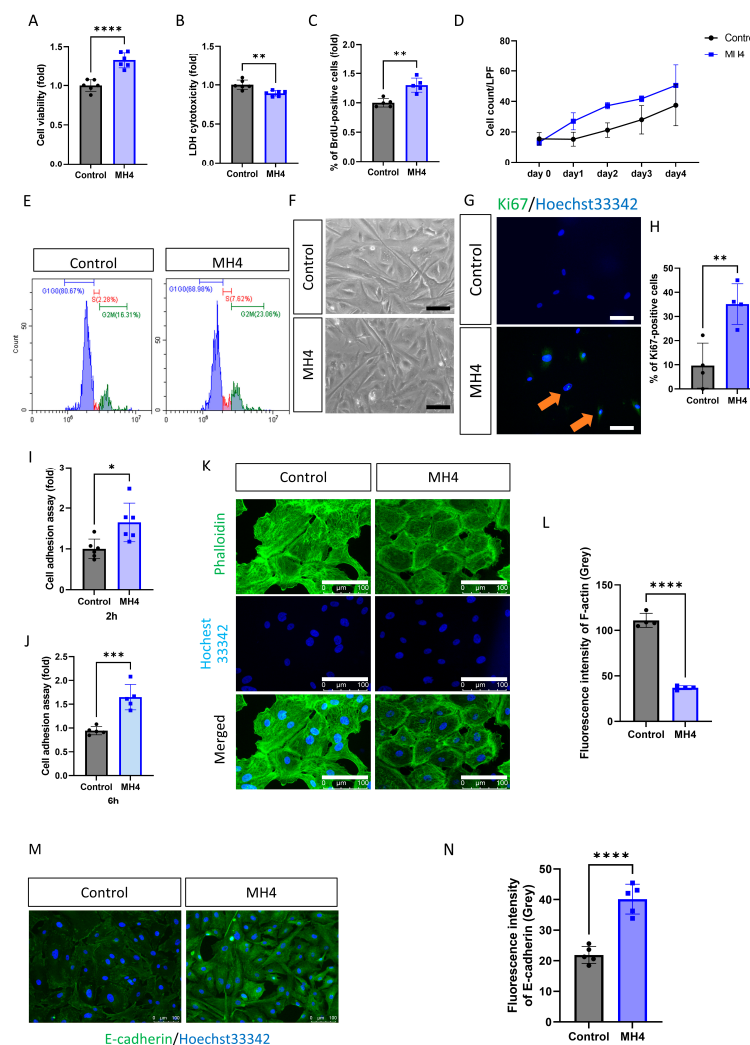


**Figure 1.** MH4 on proliferation of hCECs. (A) CCK-8 was employed to measure cell viability and (B) LDH assay was used to evaluate cytotoxicity. Proliferation rate was evaluated using BrdU proliferation assay (C), cell growth curve (D), cell cycle analysis (E), cell shape (F), and immunofluorescence staining of Ki67 (G,H). scale bar = 100  $\mu$ m. (I,J) Cell adhesion assay was performed at 2 h and 6 h using crystal violet assay. (K,L) Actin filaments arrangement was assessed by phalloidin. (M,N) Immunofluorescence staining of E-cadherin was performed. E-cadherin (green) and nucleus (blue) was observed. Scale bar = 100  $\mu$ m. \*  $p < 0.05$ , \*\*  $p < 0.01$ , \*\*\*  $p < 0.001$  and \*\*\*\*  $p < 0.0001$  by Student's *t*-test.

### 3.2. MH4 Affects Transcriptome

Transcriptome analysis was performed using NGS sequencing in order to identify differentially expressed genes (DEGs) and explore the gene expression patterns in a specific biological sample or condition [49]. Transcriptome analysis provides valuable insights into the overall gene expression profile and allows for the identification of genes that are upregulated or downregulated in response to MH4 [49]. The DEGs of MH4-treated cells are described in Table 1. A volcano plot and smear diagram of DEG levels are shown in Figure 2A,B. Molecular function of Gene Ontology is shown in Figure 2C and Table 2. TGFBR2 signaling, phosphatidyl phospholipase B activity, and nucleobase transmembrane transporter activity are involved.

**Table 1.** The differentially expressed genes of MH4-treated cells.

Gene_Symbol	Log <sub>2</sub> (Fold Change)	p-Value
ZASP	−14.838634	0.01148286
GPAA1P2	−13.510711	0.00240992
DNAAF4	−13.311489	$8.1673 \times 10^{-8}$
SAXO1	−6.902963	0.01484039
MYOCD	−6.464285	0.0055486
PTGES3L-AARSD1	−6.338733	$9.6461 \times 10^{-5}$
ADORA2A	−5.373636	0.04736651
PATE2	−5.199964	0.02142765
MSH5	−4.751082	$8.706 \times 10^{-6}$
FAM24B-CUZD1	−4.147423	0.02095992
TIAF1	−3.838953	0.00654774
ARPC4-TTLL3	−3.791950	0.00029708
C8orf44-SGK3	−3.772787	$9.2783 \times 10^{-5}$
ISY1-RAB43	−3.712475	0.04409871
LOC105378797	−3.593747	0.045978
P2RX5-TAX1BP3	−3.218089	0.00027309
C5AR2	−2.878390	0.00391602
TIMM23B-AGAP6	−2.714220	$2.1765 \times 10^{-7}$
SLC25A21	−2.611541	0.02164787
NRK	−2.576926	0.0194514
DOK6	−2.542320	0.00346687
SLCO1C1	−2.479595	0.00214007
PCK1	−2.420558	0.01594034
TMEM63C	−2.297802	0.01672008
ETNPPL	−2.187381	0.03434799
HTD2	−2.133264	$4.9329 \times 10^{-6}$
SOX5	−2.123541	0.00893952
KIF15	−2.104287	0.04083181
SH3BGR	−2.064287	0.02573281
SLC25A18	−2.012335	0.02834259
HYI	2.044232	0.03988956
RN7SL1	2.079884	0.00071722

**Table 1.** *Cont.*

Gene_Symbol	Log <sub>2</sub> (Fold Change)	p-Value
KLF2	2.194291	$6.3451 \times 10^{-5}$
ARHGAP5-AS1	2.329404	0.01048538
LRP2BP	2.349269	0.04300054
ZNF660-ZNF197	2.414622	0.01050856
SLC28A3	2.491094	0.02788002
VSTM5	2.679670	0.02360022
AMH	2.809669	0.03933912
ATRIP-TREX1	3.234381	$9.2542 \times 10^{-5}$
LRRC24	3.304932	0.00174921
MIR3648-2	3.799961	0.02673754
PPIP5K1P1	3.945428	0.00031678
GJA9-MYCBP	3.971132	0.01389741
DND1P1	3.995776	0.03677869
RPL12P16	4.074142	0.04330437
PLA2G4B	4.115890	0.04071125
NTAN1P2	4.394379	0.0286182
TMEM189-UBE2V1	5.555917	0.00099753
POC1B-GALNT4	5.621313	0.0364042
ZNF559-ZNF177	5.670612	0.00317011
FCF1P2	9.103486	0.03986722
STAG3L3	15.482174	0.04594955
RAD51L3-RFFL	16.348993	$8.243 \times 10^{-8}$
SETP17	17.898637	0.02859499
TVP23C-CDRT4	23.915473	0.01678133

**Table 2.** Molecular function of Gene Ontology by MH4.

	ID	Name	p-Value	FDR B and H	FDR B and Y	Bonferroni
1	GO:0008903	Hydroxypyruvate isomerase activity	$6.030 \times 10^{-4}$	$2.291 \times 10^{-2}$	$1.126 \times 10^{-1}$	$4.583 \times 10^{-2}$
2	GO:0015390	Purine-specific nucleoside:sodium symporter activity	$6.030 \times 10^{-4}$	$2.291 \times 10^{-2}$	$1.126 \times 10^{-1}$	$4.583 \times 10^{-2}$
3	GO:0015391	Nucleobase:monoatomic cation symporter activity	$2.409 \times 10^{-3}$	$3.589 \times 10^{-2}$	$1.764 \times 10^{-1}$	$1.831 \times 10^{-1}$
4	GO:0015389	Pyrimidine- and adenosine-specific:sodium symporter activity	$2.409 \times 10^{-3}$	$3.589 \times 10^{-2}$	$1.764 \times 10^{-1}$	$1.831 \times 10^{-1}$
5	GO:0005415	Nucleoside:sodium symporter activity	$2.409 \times 10^{-3}$	$3.589 \times 10^{-2}$	$1.764 \times 10^{-1}$	$1.831 \times 10^{-1}$
6	GO:0016861	Intramolecular oxidoreductase activity, interconverting aldoses and ketoses	$3.611 \times 10^{-3}$	$3.589 \times 10^{-2}$	$1.764 \times 10^{-1}$	$2.744 \times 10^{-1}$
7	GO:0015213	Uridine transmembrane transporter activity	$3.611 \times 10^{-3}$	$3.589 \times 10^{-2}$	$1.764 \times 10^{-1}$	$2.744 \times 10^{-1}$
8	GO:0005350	Pyrimidine nucleobase transmembrane transporter activity	$4.212 \times 10^{-3}$	$3.589 \times 10^{-2}$	$1.764 \times 10^{-1}$	$3.201 \times 10^{-1}$



Table 2. Cont.

	ID	Name	p-Value	FDR B and H	FDR B and Y	Bonferroni
9	GO:0015214	Pyrimidine nucleoside transmembrane transporter activity	$4.812 \times 10^{-3}$	$3.589 \times 10^{-2}$	$1.764 \times 10^{-1}$	$3.657 \times 10^{-1}$
10	GO:0005345	Purine nucleobase transmembrane transporter activity	$6.012 \times 10^{-3}$	$3.589 \times 10^{-2}$	$1.764 \times 10^{-1}$	$4.569 \times 10^{-1}$
11	GO:0005337	Nucleoside transmembrane transporter activity	$6.012 \times 10^{-3}$	$3.589 \times 10^{-2}$	$1.764 \times 10^{-1}$	$4.569 \times 10^{-1}$
12	GO:0005114	Type II transforming growth factor beta receptor binding	$6.611 \times 10^{-3}$	$3.589 \times 10^{-2}$	$1.764 \times 10^{-1}$	$5.024 \times 10^{-1}$
13	GO:0102545	Phosphatidyl phospholipase B activity	$6.611 \times 10^{-3}$	$3.589 \times 10^{-2}$	$1.764 \times 10^{-1}$	$5.024 \times 10^{-1}$
14	GO:0015205	Nucleobase transmembrane transporter activity	$6.611 \times 10^{-3}$	$3.589 \times 10^{-2}$	$1.764 \times 10^{-1}$	$5.024 \times 10^{-1}$

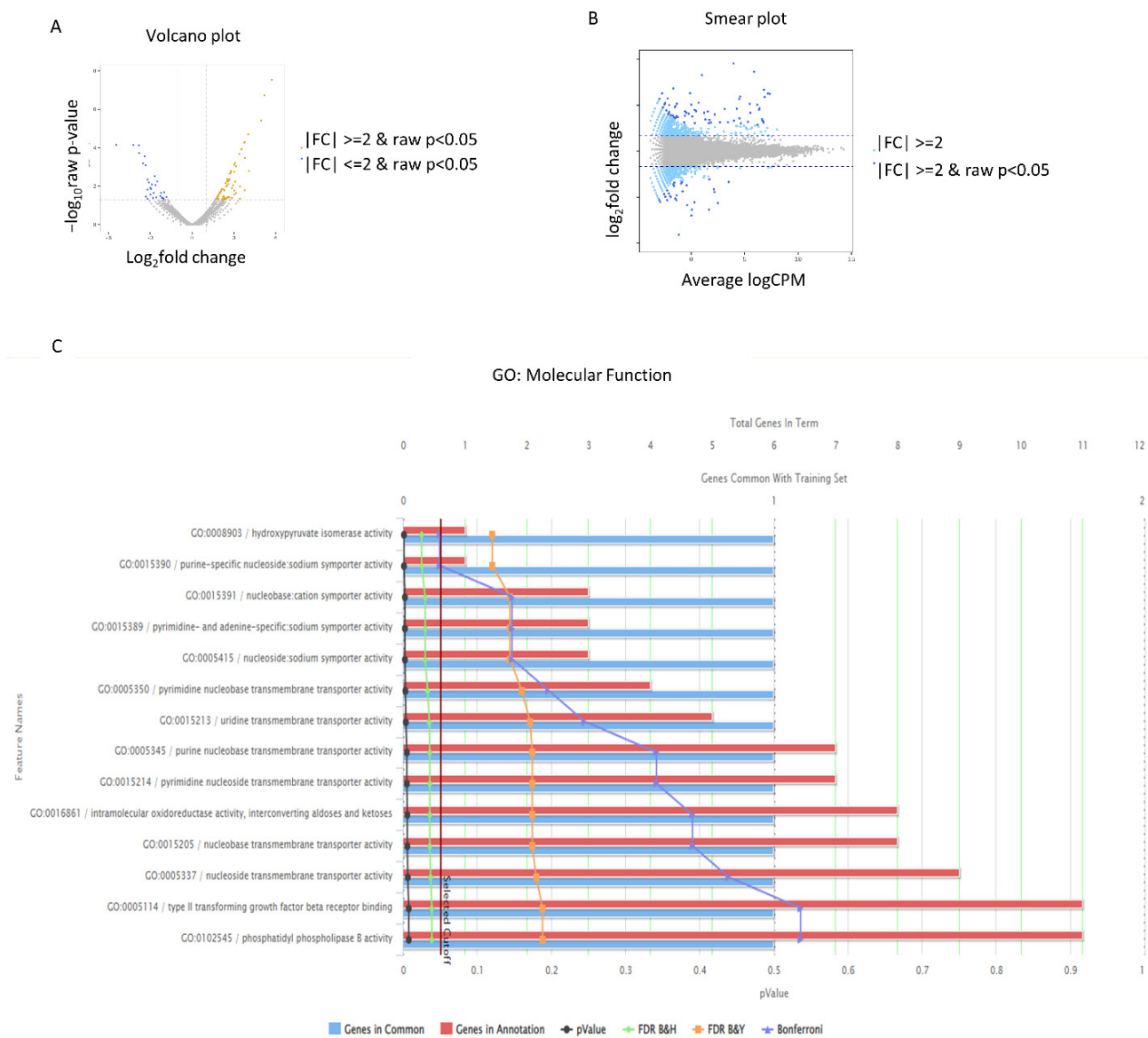


Figure 2. MH4 on proliferation of hCECs. (A,B) Volcano plot and smear plot are shown. (C) Molecular function of Gene Ontology is shown.

### 3.3. MH4 Protects the Cultured hCECs against TGF- $\beta$ -Induced Senescence

To evaluate the effect of MH4 on TGF- $\beta$ -induced senescence, RhoA, ROCK1, and ROCK2 levels were evaluated as the non-canonical pathway of the TGF- $\beta$  signaling pathway. TGF- $\beta$  elevates pRhoA and ROCK2 levels (Figure 3A,B), which are attenuated by MH4. TGF- $\beta$  decreases cell viability and increases LDH cytotoxicity; however, these effects are reversed by MH4 (Figure 3C,D). To evaluate the effect of MH4 on TGF- $\beta$ -induced senescence, cell growth curve analysis was conducted. Cell growth curve reveals the growth arrest in TGF- $\beta$ -treated cells, which is ameliorated by MH4 (Figure 3E). The cell size increases after TGF- $\beta$  treatment, which is attenuated by MH4 (Figure 3F,G). Furthermore, TGF- $\beta$  increases the percentage of SA- $\beta$ -gal-positive cells (Figure 3H,I), and mRNA expressions of *p21*, *H2Ax*, and *CDKN2A*, which is reversed by MH4 (Figure 3J–L). Intracellular oxidative stress levels are elevated by TGF- $\beta$ , which is attenuated by MH4 (Figure 3M,N).

To evaluate the effect of MH4 on the senescence-associated pathway, NF- $\kappa$ B signaling was assessed. TGF- $\beta$  promotes the nuclear translocation of NF- $\kappa$ B (Figure 4A–C). NF- $\kappa$ B activation is linked to mitochondrial dysfunction [50]. Thus, mitochondrial membrane potential was assessed. TGF- $\beta$  decreases the mitochondrial membrane potential, while MH4 ameliorates the mitochondrial membrane potential (Figure 4D–F). Lysosomes are more prominent and autophagy increases after TGF- $\beta$  treatment, which is one of the feature of senescent cells [51]; however, these effects are ameliorated by MH4 (Figure 4G,H). LC3II levels, a marker of autophagy [52], are elevated after TGF- $\beta$  treatment, but suppressed by MH4 (Figure 4I). Furthermore, *BAX* mRNA expressions are elevated after TGF- $\beta$  treatment, but suppressed by MH4 (Figure 4J). *BAX* is required for autophagy [53].

### 3.4. MH4 Protects the Cultured hCECs against Oxidative-Stress-Induced Senescence

H<sub>2</sub>O<sub>2</sub> has been reported to modulate TGF- $\beta$  signaling transduction and H<sub>2</sub>O<sub>2</sub> is generated in TGF- $\beta$  signaling transduction [54]. Thus, we evaluated whether MH4 could protect the HCECs against H<sub>2</sub>O<sub>2</sub>-induced senescence. H<sub>2</sub>O<sub>2</sub> treatment elevates pRhoA and ROCK2 levels, which are members of the non-canonical pathway of TGF- $\beta$  and attenuated by MH4 (Figure 5A,B). H<sub>2</sub>O<sub>2</sub> treatment decreases the cell viability and increases LDH cytotoxicity, both of which are ameliorated by MH4 (Figure 5C,D). The cell growth curve reveals the growth arrest, a hallmark of senescence, in H<sub>2</sub>O<sub>2</sub>-treated cells, which is ameliorated by MH4 (Figure 5E). Moreover, the cell size is increased by H<sub>2</sub>O<sub>2</sub>, but decreased by MH4 (Figure 5F,G). Similarly, the percentage of SA- $\beta$ -gal-positive cells is elevated by H<sub>2</sub>O<sub>2</sub> treatment, but reduced by MH4 (Figure 5H,I). mRNA expressions of *p21*, *H2Ax*, and *CDKN2A* are increased by H<sub>2</sub>O<sub>2</sub> treatment, which is ameliorated by MH4 (Figure 5J–L). Intracellular oxidative stress levels are increased by H<sub>2</sub>O<sub>2</sub> treatment, but reduced by MH4 (Figure 5H,I).

Furthermore, we evaluated the effect of MH4 on H<sub>2</sub>O<sub>2</sub>-induced cellular pathologic responses. H<sub>2</sub>O<sub>2</sub> treatment promotes the nuclear translocation of NF- $\kappa$ B, which is attenuated by MH4 (Figure 6A–C). H<sub>2</sub>O<sub>2</sub> decreases the mitochondrial membrane potential, while MH4 reverses this effect (Figure 6D–F). H<sub>2</sub>O<sub>2</sub> increases lysosomes and autophagy, but is ameliorated by MH4 (Figure 6G,H). LC3II levels, a marker of autophagy, are elevated by H<sub>2</sub>O<sub>2</sub>, but suppressed by MH4 (Figure 6I). Additionally, *BAX* mRNA expressions are elevated by H<sub>2</sub>O<sub>2</sub>, but suppressed by MH4 (Figure 6J).

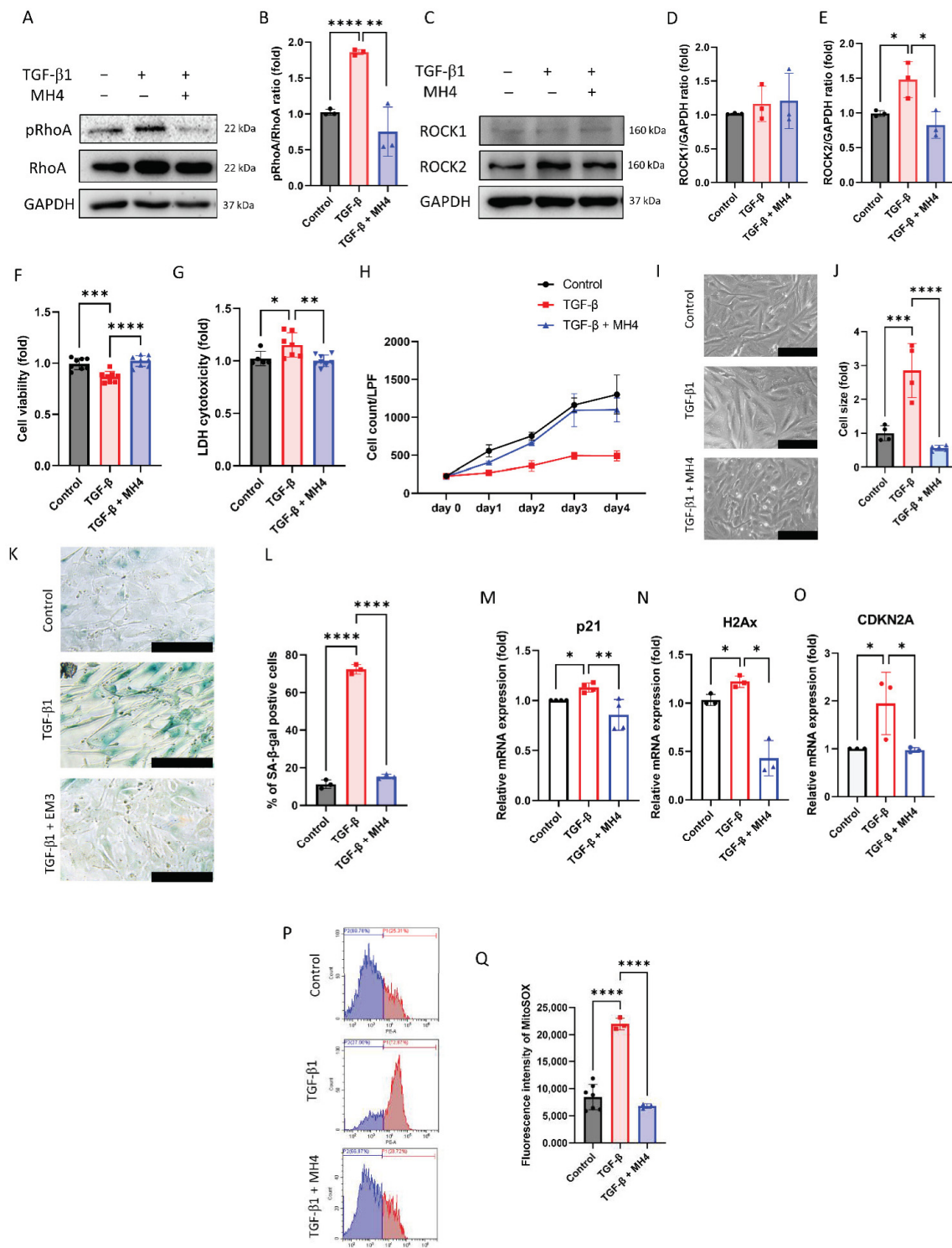


**Figure 3.** Effect of MH4 on TGF-β-induced senescence. (A,B) pRhoA and RhoA levels are evaluated using Western blot. (C,D,E) ROCK1 and ROCK2 levels are evaluated using Western blot. (F) Cell viability is conducted by CCK-8. (G) LDH cytotoxicity. (H) Comparison of cell growth curve in cells with or without TGF-β or MH4. (I,J) Cell shape and cell size are evaluated by inverted microscopy. Scale bar = 250 μm. (K,L) Senescence-β-galactosidase staining is conducted and blue indicates the positivity of senescence-β-galactosidase. Scale bar = 100 μm. (M–O) mRNA expressions of *p21*, *H2Ax*, and *CDKN2A* are measured using RT-qPCR. (P,Q) Mitochondrial oxidative stress levels are measured using MitoSOX probe. Data are expressed as mean ± S.D. \*  $p < 0.05$ , \*\*  $p < 0.01$ , \*\*\*  $p < 0.001$ , and \*\*\*\*  $p < 0.0001$  by ANOVA, followed by Tukey's test.

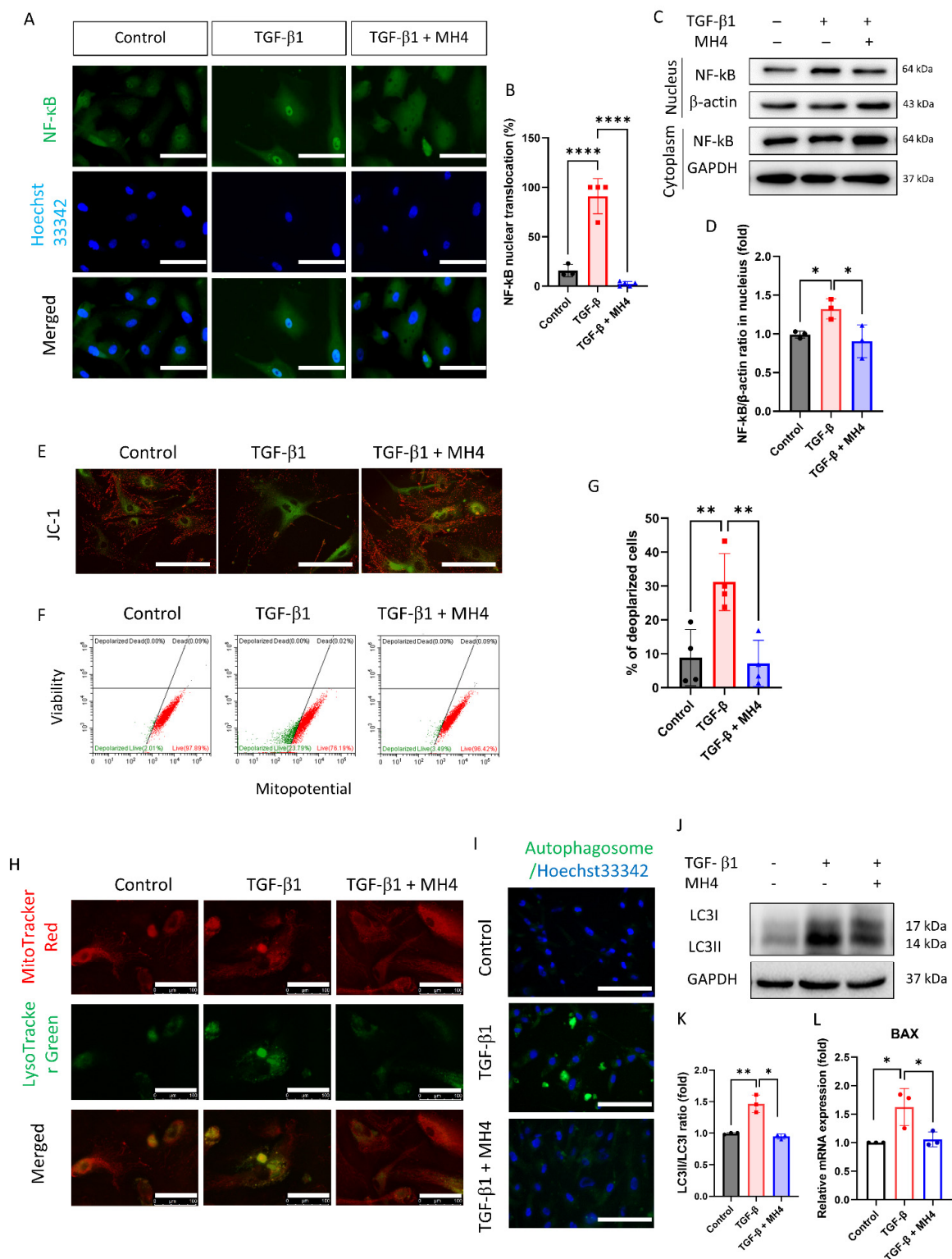


**Figure 4.** Effect of MH4 on TGF- $\beta$ -induced mitochondrial membrane potential depolarization and autophagy. (A–D) Nuclear factor- $\kappa$ B (NF- $\kappa$ B) nuclear translocation. Scale bar = 100  $\mu$ m. (E) JC-1 probe is employed to obtain the images of mitochondrial membrane potential. Scale bar = 100  $\mu$ m. (F,G) Mitopotential kit is used to evaluate mitochondrial membrane potential depolarization. (H) Lysosomes are evaluated using LysoTracker green. Scale bar = 100  $\mu$ m. (I) Autophagosome is demonstrated using autophagy detection kit. Scale bar = 100  $\mu$ m. (J,K) LC3II is evaluated by Western blotting. (L) mRNA expressions of *BAX* are evaluated by RT-qPCR. Data are expressed as mean  $\pm$  S.D. \*  $p$  < 0.05, \*\*  $p$  < 0.01, and \*\*\*\*  $p$  < 0.0001 by ANOVA, followed by Tukey's test.



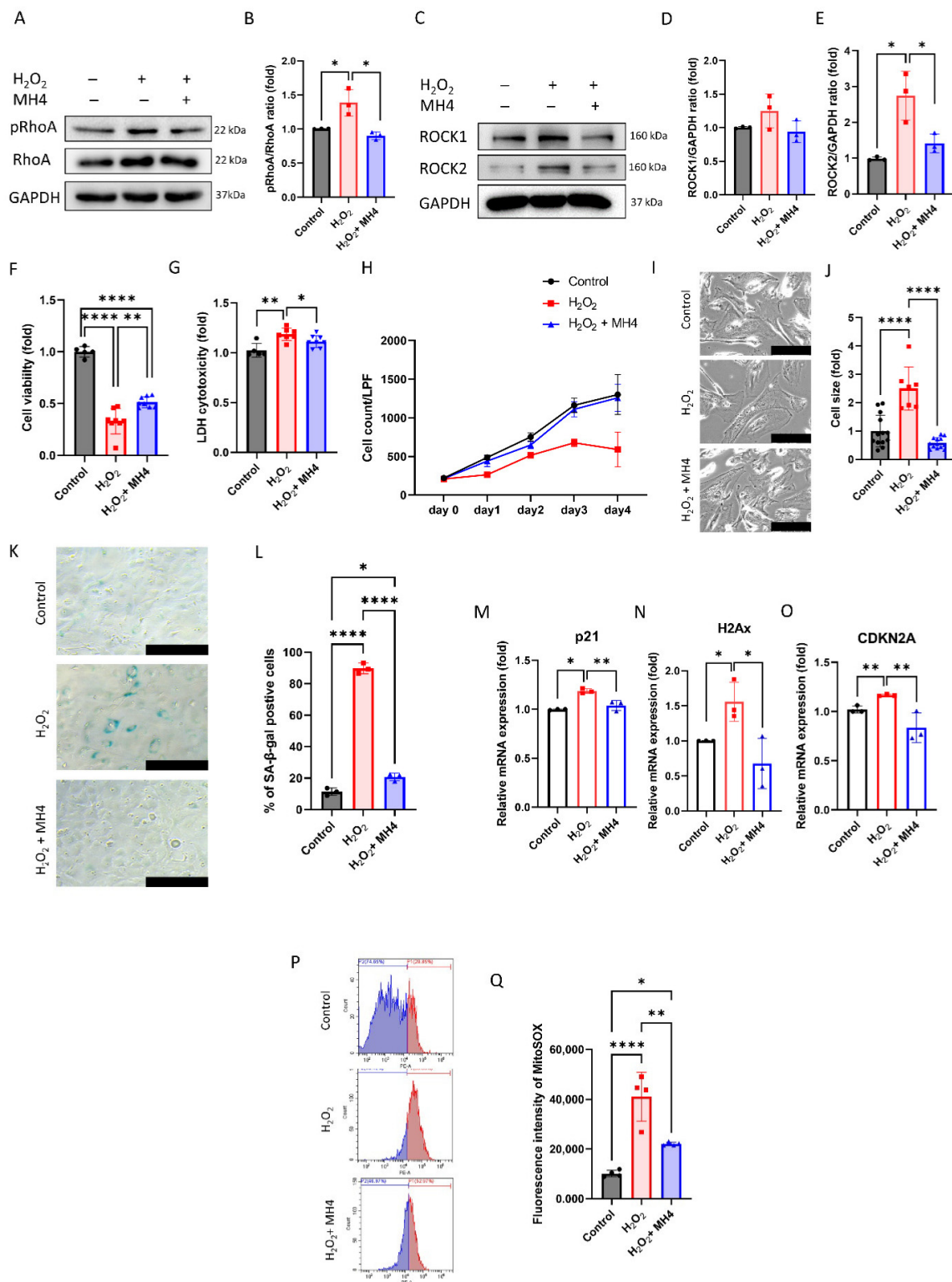


**Figure 5.** Effect of MH4 on H<sub>2</sub>O<sub>2</sub>-induced senescence. (A,B) pRhoA and RhoA levels evaluated using Western blot. (C–E) ROCK1 and ROCK2 levels evaluated using Western blot. (F) Cell viability by CCK-8 assay. (G) LDH cytotoxicity. (H) Comparison of cell growth curve in cells with or without H<sub>2</sub>O<sub>2</sub> or MH4. (I,J) Cell shape and cell size evaluated by inverted microscopy. Scale bar = 100 μm (K,L) Senescence-β-galactosidase staining is conducted and blue indicates the positivity of senescence-β-galactosidase. Scale bar = 100 μm. (M–O) mRNA expressions of *p21*, *H2Ax*, and *CDKN2A* measured using RT-qPCR. (P,Q) Mitochondrial oxidative stress levels measured using MitoSOX probe. Data are expressed as mean ± S.D. \* *p* < 0.05, \*\* *p* < 0.01, and \*\*\*\* *p* < 0.0001 by ANOVA, followed by Tukey's test.

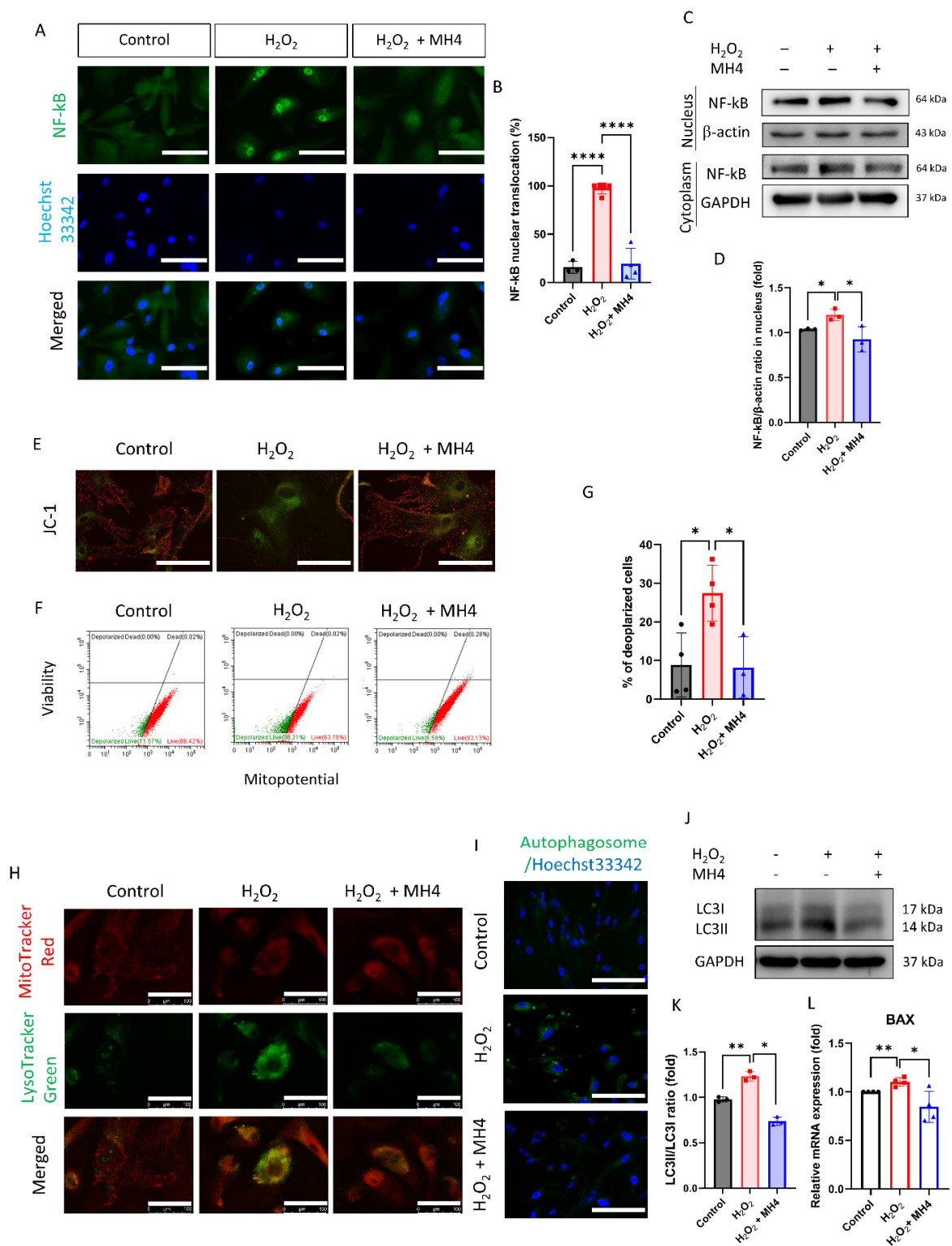


**Figure 6.** Effect of MH4 on H<sub>2</sub>O<sub>2</sub>-induced mitochondrial membrane potential depolarization and autophagy. (A–D) Nuclear factor-κB (NF-κB) nuclear translocation. Scale bar = 100 μm. (E) JC-1 probe used to evaluate the mitochondrial membrane potential. Scale bar = 100 μm. (F,G) MitoPotential kit used to evaluate mitochondrial membrane potential depolarization. (H) Lysosome evaluated using LysoTracker green. Scale bar = 100 μm. (I) Autophagosome is demonstrated using autophagy detection kit. Scale bar = 100 μm. (J,K) LC3II evaluated by Western blotting. (L) mRNA expressions of BAX evaluated by RT-qPCR. Data are expressed as mean ± S.D. \* *p* < 0.05, \*\* *p* < 0.01, and \*\*\*\* *p* < 0.0001 by ANOVA, followed by Tukey's test.

#### 4. Discussion

Corneal endothelial cells (CECs), which are located at the innermost layer of the cornea and dehydrate the corneal stroma, are different from vascular endothelial cells [55]. CECs originate from neural crest cells [55]. TGF- $\beta$  is a multifunctional cytokine that plays a crucial role in regulating cell growth, differentiation, migration, and survival [20,56]. In many cell types, TGF- $\beta$  signaling can inhibit cell proliferation including in hCECs through Rho/ROCK signaling [3,20]. Rho/ROCK signaling is a pathway that regulates actin cytoskeleton dynamics, cell proliferation, migration, and adhesion [57]. Inhibition of Rho/ROCK signaling has been shown to promote hCEC proliferation [58]. TGF- $\beta$  binds to the TGF- $\beta$  receptor, and then TGFBR2 activates RhoA, which subsequently activates ROCK1 and ROCK2 [59]. It has been suggested that p-Tyr42 on RhoA may play a role in regulating TGF- $\beta$  signaling and its downstream effects on transcription regulation [59]. In this study, we reveal that MH4, a p-Tyr42 RhoA inhibitor, promotes the regeneration of hCECs. ROCK inhibitors, such as Y27632 and fasudil, promote the proliferation of hCECs [58,60,61] by facilitating the degradation of p27Kip1 (p27), promoting the cyclin D levels [61], and inducing the loss of actin stress fibers and cell–cell tight junctions [58]. The shape of CECs is restored after treating with ROCK inhibitors [58]. p-Tyr42 RhoA is a protein upstream of ROCK [35]. p-Tyr42 RhoA inhibition selectively suppresses the activated form of RhoA and, subsequently, inhibits ROCK2 [35], which is necessary for the stabilization of the actin cytoskeleton by modulating cofilin phosphorylation [30]. ROCK2 is preferentially activated by p-Tyr42 RhoA [34]. F-actin attenuation is associated with proliferation in CECs different from vascular endothelial cells [58]. F-actin filaments are involved in the formation of cellular protrusions called filopodia, which are important for cell migration and the formation of new blood vessels [62].

Transcriptome analysis shows that MH4 has an effect on TGF- $\beta$  signaling, hydroxypyruvate isomerase, and nuclear transmembrane transporters. Hydroxypyruvate isomerase is an enzyme involved in the conversion of hydroxypyruvate to pyruvate, a key step in energy metabolism [63]. Changes in hydroxypyruvate isomerase activity may impact cellular energy production and metabolic pathways. Nuclear transmembrane transporters are responsible for the movement of molecules across the nuclear envelope, regulating the exchange of proteins, nucleic acids, and other molecules between the cytoplasm and the nucleus [64]. Changes in the activity of nuclear transmembrane transporters can have broad implications for cellular processes such as gene expression, DNA replication, and cellular signaling [65,66]. MH4 may translocate the signaling molecules across the nuclear transmembrane into the nucleus via these nuclear transmembrane transporters.

To investigate whether the failure of cells to regenerate is due to senescence or failure to proliferate, the number of cultured cells overtime was assessed and cell growth curve was added. It is confirmed that cell growth stops when treated with TGF- $\beta$  and H<sub>2</sub>O<sub>2</sub>, which is regarded as senescence. CECs undergo senescence with age, which is involved in CDKN2A and p53 signaling pathways [20,67,68]. TGF- $\beta$  has been reported to induce senescence in CECs [20,56]. In this study, MH4 suppresses TGF- $\beta$ -induced senescence by regulating the ROS/NF- $\kappa$ B signaling pathway. TGF- $\beta$  accelerates or causes senescence and senescence-related phenotypes in a variety of cells [11,20]. A variety of signaling pathways, including ROS, p53, and NF- $\kappa$ B, are involved in TGF- $\beta$ -induced senescence [69–71]. TGF- $\beta$  promotes ROS production in the mitochondria in several cell types [72,73]. ROS modify histones and DNA by participating in interconnected epigenetic phases and contribute to the onset and progression of cellular senescence by directly damaging mtDNA [74]. TGF- $\beta$  signaling can activate the Rho/ROCK pathway linking NF- $\kappa$ B translocation into the nucleus [75,76]. NF- $\kappa$ B is activated during senescence and induces the secretion of senescence-associated secretory phenotype (SASP) factors, which are mainly inflammatory cytokines [71].

This study reveals that MH4 ameliorates TGF- $\beta$ -induced mitochondrial depolarization and autophagy. The depolarization of mitochondrial membrane potential is linked to mitochondrial dysfunction because the maintenance of the membrane potential is required to generate energy in the mitochondria [77]. Loss of mitochondrial membrane potential results

in a deprivation of cellular energy, reducing the cell viability, and causing cell death [78]. Autophagy is considered a cell survival and death mechanism and regulates the number and health of mitochondria [79]. Mitochondrial proteins are degraded by autophagy in aged cells [80]. Although autophagy redeems defects in mitochondrial dynamics by blocking mitochondrial fission, mitochondrial autophagy is induced for selective clearance of damaged mitochondria in cells [81,82]. TGF- $\beta$  induces depolarization of mitochondrial membrane potential and autophagy by elevating mitochondrial ROS levels [83,84].

As TGF- $\beta$  increases ROS in hCECs, we investigate whether MH4 attenuates the effect of oxidative stress. Oxidative stress has been reported as a major cause of senescence [85,86]. In this study, MH4 inhibits H<sub>2</sub>O<sub>2</sub>-induced senescence by regulating the ROS/NF- $\kappa$ B signaling pathway. Exogenous H<sub>2</sub>O<sub>2</sub> is used to generate ROS, which reduces cell viability and increases intracellular oxidative stress levels [87], although ROS is mainly produced as byproducts of mitochondrial metabolism or is specifically generated by several oxidases, such as nicotinamide adenine dinucleotide phosphate oxidase (NOX) [88,89]. Oxidative stress increases the expression of ROCK2, which is involved in the main pathway through which TGF- $\beta$  activates NF- $\kappa$ B [15]. p-Tyr42 RhoA, which is upstream of ROCK2 and the active form of RhoA, is translocated into the nucleus and elevates NOX expression, which results in an increase in ROS levels and senescence [90]. Exogenous H<sub>2</sub>O<sub>2</sub> induces senescence and activates NF- $\kappa$ B translocation into the nucleus [91]. NF- $\kappa$ B is involved in senescence and induces the release of senescence-associated secretory phenotype (SASP) factors, including IL-1 $\beta$ , IL-6, IL-8, TNF- $\alpha$ , and MMPs [71], which contributes to the senescence of adjacent cells [92]. This study shows that MH4 ameliorates H<sub>2</sub>O<sub>2</sub>-induced mitochondrial depolarization and autophagy. ROS and oxidative stress are involved in the recruitment of mitophagy proteins [93]. Mitochondrial damage and loss of energy-generating capacity are characteristics of aged cells [79]. RhoA/ROCK2, which is activated by ROS, mediates mitochondrial functions, autophagy, and actin dynamics [26,94,95]. p-Tyr42 RhoA inhibition by MH4 attenuates this process.

In conclusion, MH4, a p-Tyr42 RhoA inhibitor, promotes the regeneration of hCECs and protects them against TGF- $\beta$ - and H<sub>2</sub>O<sub>2</sub>-induced senescence via the ROS/NF- $\kappa$ B/mitochondrial pathway.

**Supplementary Materials:** The following supporting information can be downloaded at: <https://www.mdpi.com/article/10.3390/antiox12061186/s1>, Table S1: Primers for RT-PCR.

**Author Contributions:** Conceptualization, data curation, investigation, and resources, J.S.H., S.-H.O., K.B.N. and Y.J.S.; methodology, software, validation, and formal analysis, H.J.K. and Y.J.S.; writing—original draft preparation, H.J.K., J.S.H. and Y.J.S.; writing—review and editing, Y.J.S.; visualization, H.J.K., S.-H.O., K.B.N. and J.S.H.; supervision, J.-B.P.; project administration and funding acquisition, Y.J.S. All authors have read and agreed to the published version of the manuscript.

**Funding:** This study was supported by Hallym University Medical Center Research Fund funded by Hallym University Medical Center and the National Research Foundation (NRF) grant (NRF-2023R1A2C2002674) funded by the Korean government.

**Institutional Review Board Statement:** This study was approved by the Institutional Review Board of Kangnam Sacred Heart Hospital (approval number: NON2022-006).

**Informed Consent Statement:** Not Applicable.

**Data Availability Statement:** The datasets are available from corresponding author on reasonable request.

**Conflicts of Interest:** Jae-bong Park owns shares in the ELMED company. The other authors have no conflict of interest. The funders had no role in the design of the study; in the collection, analyses, or interpretation of data; in the writing of the manuscript; or in the decision to publish the results.



## References

- Weant, J.; Eveleth, D.D.; Subramaniam, A.; Jenkins-Eveleth, J.; Blaber, M.; Li, L.; Ornitz, D.M.; Alimardanov, A.; Broadt, T.; Dong, H.; et al. Regenerative responses of rabbit corneal endothelial cells to stimulation by fibroblast growth factor 1 (FGF1) derivatives, TTHX1001 and TTHX1114. *Growth Factors* **2021**, *39*, 14–27. [\[CrossRef\]](#) [\[PubMed\]](#)
- Kumar, A.; Yun, H.; Funderburgh, M.L.; Du, Y. Regenerative therapy for the Cornea. *Prog. Retin. Eye Res.* **2022**, *87*, 101011. [\[CrossRef\]](#) [\[PubMed\]](#)
- Miyagi, H.; Kim, S.; Li, J.; Murphy, C.J.; Thomasy, S.M. Topical Rho-Associated Kinase Inhibitor, Y27632, Accelerates Corneal Endothelial Regeneration in a Canine Cryoinjury Model. *Cornea* **2019**, *38*, 352–359. [\[CrossRef\]](#) [\[PubMed\]](#)
- Okumura, N.; Koizumi, N.; Ueno, M.; Sakamoto, Y.; Takahashi, H.; Tsuchiya, H.; Hamuro, J.; Kinoshita, S. ROCK inhibitor converts corneal endothelial cells into a phenotype capable of regenerating in vivo endothelial tissue. *Am. J. Pathol.* **2012**, *181*, 268–277. [\[CrossRef\]](#)
- Lee, J.; Park, S.; Roh, S. Y-27632, a ROCK inhibitor, delays senescence of putative murine salivary gland stem cells in culture. *Arch. Oral. Biol.* **2015**, *60*, 875–882. [\[CrossRef\]](#)
- Jung, B.; Lee, H.; Kim, S.; Tchah, H.; Hwang, C. Effect of Rho-Associated Kinase Inhibitor and Mesenchymal Stem Cell-Derived Conditioned Medium on Corneal Endothelial Cell Senescence and Proliferation. *Cells* **2021**, *10*, 1463. [\[CrossRef\]](#)
- He, Z.; Forest, F.; Gain, P.; Rageade, D.; Bernard, A.; Acquart, S.; Peoc'h, M.; Defoe, D.M.; Thuret, G. 3D map of the human corneal endothelial cell. *Sci. Rep.* **2016**, *6*, 29047. [\[CrossRef\]](#)
- Wang, H.; Yan, S.; Chai, H.; Riha, G.M.; Li, M.; Yao, Q.; Chen, C. Shear stress induces endothelial transdifferentiation from mouse smooth muscle cells. *Biochem. Biophys. Res. Commun.* **2006**, *346*, 860–865. [\[CrossRef\]](#)
- Kruger-Genge, A.; Blocki, A.; Franke, R.P.; Jung, F. Vascular Endothelial Cell Biology: An Update. *Int. J. Mol. Sci.* **2019**, *20*, 4411. [\[CrossRef\]](#)
- Roy, O.; Leclerc, V.B.; Bourget, J.M.; Theriault, M.; Proulx, S. Understanding the process of corneal endothelial morphological change in vitro. *Investig. Ophthalmol. Vis. Sci.* **2015**, *56*, 1228–1237. [\[CrossRef\]](#)
- Tominaga, K.; Suzuki, H.I. TGF-beta Signaling in Cellular Senescence and Aging-Related Pathology. *Int. J. Mol. Sci.* **2019**, *20*, 5002. [\[CrossRef\]](#)
- Kumper, S.; Mardakheh, F.K.; McCarthy, A.; Yeo, M.; Stamp, G.W.; Paul, A.; Worboys, J.; Sadok, A.; Jorgensen, C.; Guichard, S.; et al. Rho-associated kinase (ROCK) function is essential for cell cycle progression, senescence and tumorigenesis. *Elife* **2016**, *5*, e12994. [\[CrossRef\]](#) [\[PubMed\]](#)
- Xu, T.; Wu, M.; Feng, J.; Lin, X.; Gu, Z. RhoA/Rho kinase signaling regulates transforming growth factor-beta1-induced chondrogenesis and actin organization of synovium-derived mesenchymal stem cells through interaction with the Smad pathway. *Int. J. Mol. Med.* **2012**, *30*, 1119–1125. [\[CrossRef\]](#) [\[PubMed\]](#)
- Zanin-Zhorov, A.; Blazar, B.R. ROCK2, a critical regulator of immune modulation and fibrosis has emerged as a therapeutic target in chronic graft-versus-host disease. *Clin. Immunol.* **2021**, *230*, 108823. [\[CrossRef\]](#) [\[PubMed\]](#)
- Nagai, Y.; Matoba, K.; Kawanami, D.; Takeda, Y.; Akamine, T.; Ishizawa, S.; Kanazawa, Y.; Yokota, T.; Utsunomiya, K.; Nishimura, R. ROCK2 regulates TGF-beta-induced expression of CTGF and profibrotic genes via NF-kappaB and cytoskeleton dynamics in mesangial cells. *Am. J. Physiol.-Renal Physiol.* **2019**, *317*, F839–F851. [\[CrossRef\]](#) [\[PubMed\]](#)
- Harris, D.L.; Joyce, N.C. Transforming growth factor-beta suppresses proliferation of rabbit corneal endothelial cells in vitro. *J. Interferon Cytokine Res.* **1999**, *19*, 327–334. [\[CrossRef\]](#)
- Okumura, N.; Kay, E.P.; Nakahara, M.; Hamuro, J.; Kinoshita, S.; Koizumi, N. Inhibition of TGF-beta signaling enables human corneal endothelial cell expansion in vitro for use in regenerative medicine. *PLoS ONE* **2013**, *8*, e58000. [\[CrossRef\]](#)
- Beaulieu Leclerc, V.; Roy, O.; Santerre, K.; Proulx, S. TGF-beta1 promotes cell barrier function upon maturation of corneal endothelial cells. *Sci. Rep.* **2018**, *8*, 4438. [\[CrossRef\]](#)
- Zhang, Z.H.; Miao, Y.Y.; Ke, B.L.; Liu, K.; Xu, X. LY2109761, Transforming Growth Factor beta Receptor Type I and Type II Dual Inhibitor, is a Novel Approach to Suppress Endothelial Mesenchymal Transformation in Human Corneal Endothelial Cells. *Cell. Physiol. Biochem.* **2018**, *50*, 963–972. [\[CrossRef\]](#)
- Li, Z.; Liu, T.; Ma, J.; Guo, Q.; Ma, L.; Lv, Q.; Jiang, Y.; Wei, C.; Zhang, J. TGF-beta induces corneal endothelial senescence via increase of mitochondrial reactive oxygen species in chronic corneal allograft failure. *Aging* **2018**, *10*, 3474–3485. [\[CrossRef\]](#)
- Okumura, N.; Hashimoto, K.; Kitahara, M.; Okuda, H.; Ueda, E.; Watanabe, K.; Nakahara, M.; Sato, T.; Kinoshita, S.; Tourtas, T.; et al. Activation of TGF-beta signaling induces cell death via the unfolded protein response in Fuchs endothelial corneal dystrophy. *Sci. Rep.* **2017**, *7*, 6801. [\[CrossRef\]](#) [\[PubMed\]](#)
- Liu, J.; Gao, H.Y.; Wang, X.F. The role of the Rho/ROCK signaling pathway in inhibiting axonal regeneration in the central nervous system. *Neural Regen. Res.* **2015**, *10*, 1892–1896. [\[CrossRef\]](#) [\[PubMed\]](#)
- Haga, R.B.; Ridley, A.J. Rho GTPases: Regulation and roles in cancer cell biology. *Small GTPases* **2016**, *7*, 207–221. [\[CrossRef\]](#) [\[PubMed\]](#)
- Guo, X.; Stafford, L.J.; Bryan, B.; Xia, C.; Ma, W.; Wu, X.; Liu, D.; Songyang, Z.; Liu, M. A Rac/Cdc42-specific exchange factor, GEFT, induces cell proliferation, transformation, and migration. *J. Biol. Chem.* **2003**, *278*, 13207–13215. [\[CrossRef\]](#) [\[PubMed\]](#)
- Maldonado, M.D.M.; Medina, J.I.; Velazquez, L.; Dharmawardhane, S. Targeting Rac and Cdc42 GEFs in Metastatic Cancer. *Front. Cell Dev. Biol.* **2020**, *8*, 201. [\[CrossRef\]](#)

26. Hartmann, S.; Ridley, A.J.; Lutz, S. The Function of Rho-Associated Kinases ROCK1 and ROCK2 in the Pathogenesis of Cardiovascular Disease. *Front. Pharmacol.* **2015**, *6*, 276. [\[CrossRef\]](#)
27. Kaczorowski, M.; Biecek, P.; Donizy, P.; Pieniazek, M.; Matkowski, R.; Halon, A. ROCK1 and ROCK2 Are Down-regulated in Aggressive and Advanced Skin Melanomas—A Clinicopathological Perspective. *Anticancer. Res.* **2020**, *40*, 1931–1942. [\[CrossRef\]](#)
28. Julian, L.; Olson, M.F. Rho-associated coiled-coil containing kinases (ROCK): Structure, regulation, and functions. *Small GTPases* **2014**, *5*, e29846. [\[CrossRef\]](#)
29. Shimizu, T.; Liao, J.K. Rho Kinases and Cardiac Remodeling. *Circ. J.* **2016**, *80*, 1491–1498. [\[CrossRef\]](#)
30. Shi, J.; Wu, X.; Surma, M.; Vemula, S.; Zhang, L.; Yang, Y.; Kapur, R.; Wei, L. Distinct roles for ROCK1 and ROCK2 in the regulation of cell detachment. *Cell Death Dis.* **2013**, *4*, e483. [\[CrossRef\]](#)
31. Sunamura, S.; Satoh, K.; Kurosawa, R.; Ohtsuki, T.; Kikuchi, N.; Elias-Al-Mamun, M.; Shimizu, T.; Ikeda, S.; Suzuki, K.; Satoh, T.; et al. Different roles of myocardial ROCK1 and ROCK2 in cardiac dysfunction and postcapillary pulmonary hypertension in mice. *Proc. Natl. Acad. Sci. USA* **2018**, *115*, E7129–E7138. [\[CrossRef\]](#) [\[PubMed\]](#)
32. Okamoto, R.; Li, Y.; Noma, K.; Hiroi, Y.; Liu, P.Y.; Taniguchi, M.; Ito, M.; Liao, J.K. FHL2 prevents cardiac hypertrophy in mice with cardiac-specific deletion of ROCK2. *FASEB J.* **2013**, *27*, 1439–1449. [\[CrossRef\]](#) [\[PubMed\]](#)
33. Zhang, Y.M.; Bo, J.; Taffet, G.E.; Chang, J.; Shi, J.; Reddy, A.K.; Michael, L.H.; Schneider, M.D.; Entman, M.L.; Schwartz, R.J.; et al. Targeted deletion of ROCK1 protects the heart against pressure overload by inhibiting reactive fibrosis. *FASEB J.* **2006**, *20*, 916–925. [\[CrossRef\]](#) [\[PubMed\]](#)
34. Kim, J.G.; Mahmud, S.; Min, J.K.; Lee, Y.B.; Kim, H.; Kang, D.C.; Park, H.S.; Seong, J.; Park, J.B. RhoA GTPase phosphorylated at tyrosine 42 by src kinase binds to beta-catenin and contributes transcriptional regulation of vimentin upon Wnt3A. *Redox Biol.* **2021**, *40*, 101842. [\[CrossRef\]](#)
35. Cap, K.C.; Kim, J.G.; Hamza, A.; Park, J.B. P-Tyr42 RhoA GTPase amplifies superoxide formation through p47phox, phosphorylated by ROCK. *Biochem. Biophys. Res. Commun.* **2020**, *523*, 972–978. [\[CrossRef\]](#)
36. Kim, J.G.; Choi, K.C.; Hong, C.W.; Park, H.S.; Choi, E.K.; Kim, Y.S.; Park, J.B. Tyr42 phosphorylation of RhoA GTPase promotes tumorigenesis through nuclear factor (NF)-kappaB. *Free. Radic. Biol. Med.* **2017**, *112*, 69–83. [\[CrossRef\]](#)
37. Smeringaiova, I.; Utheim, T.P.; Jirsova, K. Ex vivo expansion and characterization of human corneal endothelium for transplantation: A review. *Stem Cell Res. Ther.* **2021**, *12*, 554. [\[CrossRef\]](#)
38. Cai, L.; Qin, X.; Xu, Z.; Song, Y.; Jiang, H.; Wu, Y.; Ruan, H.; Chen, J. Comparison of Cytotoxicity Evaluation of Anticancer Drugs between Real-Time Cell Analysis and CCK-8 Method. *ACS Omega* **2019**, *4*, 12036–12042. [\[CrossRef\]](#)
39. Yin, L.M.; Wei, Y.; Wang, W.Q.; Wang, Y.; Xu, Y.D.; Yang, Y.Q. Simultaneous application of BrdU and WST-1 measurements for detection of the proliferation and viability of airway smooth muscle cells. *Biol. Res.* **2014**, *47*, 75. [\[CrossRef\]](#)
40. Kaja, S.; Payne, A.J.; Naumchuk, Y.; Koulen, P. Quantification of Lactate Dehydrogenase for Cell Viability Testing Using Cell Lines and Primary Cultured Astrocytes. *Curr. Protoc. Toxicol.* **2017**, *72*, 2–26. [\[CrossRef\]](#)
41. Hwang, J.S.; Ma, D.J.; Choi, J.; Shin, Y.J. COL8A2 Regulates the Fate of Corneal Endothelial Cells. *Investig. Ophthalmol. Vis. Sci.* **2020**, *61*, 26. [\[CrossRef\]](#)
42. Kang, S.J.; Jun, J.S.; Hong, K.W. Transcriptome Analysis Reveals Immunomodulatory Effect of Spore-Displayed p75 on Human Intestinal Epithelial Caco-2 Cells. *Int. J. Mol. Sci.* **2022**, *23*, 14519. [\[CrossRef\]](#)
43. Bolger, A.M.; Lohse, M.; Usadel, B. Trimmomatic: A flexible trimmer for Illumina sequence data. *Bioinformatics* **2014**, *30*, 2114–2120. [\[CrossRef\]](#)
44. Kim, D.; Paggi, J.M.; Park, C.; Bennett, C.; Salzberg, S.L. Graph-based genome alignment and genotyping with HISAT2 and HISAT-genotype. *Nat. Biotechnol.* **2019**, *37*, 907–915. [\[CrossRef\]](#) [\[PubMed\]](#)
45. Love, M.I.; Huber, W.; Anders, S. Moderated estimation of fold change and dispersion for RNA-seq data with DESeq2. *Genome Biol.* **2014**, *15*, 550. [\[CrossRef\]](#)
46. Pertea, M.; Pertea, G.M.; Antonescu, C.M.; Chang, T.C.; Mendell, J.T.; Salzberg, S.L. StringTie enables improved reconstruction of a transcriptome from RNA-seq reads. *Nat. Biotechnol.* **2015**, *33*, 290–295. [\[CrossRef\]](#) [\[PubMed\]](#)
47. Chen, J.; Bardes, E.E.; Aronow, B.J.; Jegga, A.G. ToppGene Suite for gene list enrichment analysis and candidate gene prioritization. *Nucleic Acids Res.* **2009**, *37*, W305–W311. [\[CrossRef\]](#) [\[PubMed\]](#)
48. Guo, S.; Liang, Y.; Murphy, S.F.; Huang, A.; Shen, H.; Kelly, D.F.; Sobrado, P.; Sheng, Z. A rapid and high content assay that measures cyto-ID-stained autophagic compartments and estimates autophagy flux with potential clinical applications. *Autophagy* **2015**, *11*, 560–572. [\[CrossRef\]](#)
49. Xu, L.; Deng, Z.N.; Wu, K.C.; Malviya, M.K.; Solanki, M.K.; Verma, K.K.; Pang, T.; Li, Y.J.; Liu, X.Y.; Kashyap, B.K.; et al. Transcriptome Analysis Reveals a Gene Expression Pattern That Contributes to Sugarcane Bud Propagation Induced by Indole-3-Butyric Acid. *Front. Plant. Sci.* **2022**, *13*, 852886. [\[CrossRef\]](#)
50. Albensi, B.C. What Is Nuclear Factor Kappa B (NF-kappaB) Doing in and to the Mitochondrion? *Front. Cell Dev. Biol.* **2019**, *7*, 154. [\[CrossRef\]](#)
51. Aman, Y.; Schmauck-Medina, T.; Hansen, M.; Morimoto, R.I.; Simon, A.K.; Bjedov, I.; Palikaras, K.; Simonsen, A.; Johansen, T.; Tavernarakis, N.; et al. Autophagy in healthy aging and disease. *Nat. Aging* **2021**, *1*, 634–650. [\[CrossRef\]](#)
52. Yim, W.W.; Mizushima, N. Lysosome biology in autophagy. *Cell Discov.* **2020**, *6*, 6. [\[CrossRef\]](#) [\[PubMed\]](#)
53. Karch, J.; Schips, T.G.; Maliken, B.D.; Brody, M.J.; Sargent, M.A.; Kanisicak, O.; Molkentin, J.D. Autophagic cell death is dependent on lysosomal membrane permeability through Bax and Bak. *Elife* **2017**, *6*, e30543. [\[CrossRef\]](#) [\[PubMed\]](#)

54. Junn, E.; Lee, K.N.; Ju, H.R.; Han, S.H.; Im, J.Y.; Kang, H.S.; Lee, T.H.; Bae, Y.S.; Ha, K.S.; Lee, Z.W.; et al. Requirement of hydrogen peroxide generation in TGF-beta 1 signal transduction in human lung fibroblast cells: Involvement of hydrogen peroxide and Ca<sup>2+</sup> in TGF-beta 1-induced IL-6 expression. *J. Immunol.* **2000**, *165*, 2190–2197. [\[CrossRef\]](#) [\[PubMed\]](#)
55. So, S.; Park, Y.; Kang, S.S.; Han, J.; Sunwoo, J.H.; Lee, W.; Kim, J.; Ye, E.A.; Kim, J.Y.; Tchah, H.; et al. Therapeutic Potency of Induced Pluripotent Stem-Cell-Derived Corneal Endothelial-like Cells for Corneal Endothelial Dysfunction. *Int. J. Mol. Sci.* **2022**, *24*, 701. [\[CrossRef\]](#)
56. Bae, Y.; Hwang, J.S.; Shin, Y.J. miR-30c-1 encourages human corneal endothelial cells to regenerate through ameliorating senescence. *Aging* **2021**, *13*, 9348–9372. [\[CrossRef\]](#)
57. Guan, G.; Cannon, R.D.; Coates, D.E.; Mei, L. Effect of the Rho-Kinase/ROCK Signaling Pathway on Cytoskeleton Components. *Genes* **2023**, *14*, 272. [\[CrossRef\]](#)
58. Meekins, L.C.; Rosado-Adames, N.; Maddala, R.; Zhao, J.J.; Rao, P.V.; Afshari, N.A. Corneal Endothelial Cell Migration and Proliferation Enhanced by Rho Kinase (ROCK) Inhibitors in In Vitro and In Vivo Models. *Investig. Ophthalmol. Vis. Sci.* **2016**, *57*, 6731–6738. [\[CrossRef\]](#)
59. Kim, J.G.; Islam, R.; Cho, J.Y.; Jeong, H.; Cap, K.C.; Park, Y.; Hossain, A.J.; Park, J.B. Regulation of RhoA GTPase and various transcription factors in the RhoA pathway. *J. Cell. Physiol.* **2018**, *233*, 6381–6392. [\[CrossRef\]](#)
60. Lee, W.; Miyagawa, Y.; Long, C.; Zhang, M.; Cooper, D.K.; Hara, H. Effect of Rho-kinase Inhibitor, Y27632, on Porcine Corneal Endothelial Cell Culture, Inflammation and Immune Regulation. *Ocul. Immunol. Inflamm.* **2016**, *24*, 579–593. [\[CrossRef\]](#)
61. Okumura, N.; Nakano, S.; Kay, E.P.; Numata, R.; Ota, A.; Sowa, Y.; Sakai, T.; Ueno, M.; Kinoshita, S.; Koizumi, N. Involvement of cyclin D and p27 in cell proliferation mediated by ROCK inhibitors Y-27632 and Y-39983 during corneal endothelium wound healing. *Investig. Ophthalmol. Vis. Sci.* **2014**, *55*, 318–329. [\[CrossRef\]](#) [\[PubMed\]](#)
62. Blanchoin, L.; Boujemaa-Paterski, R.; Sykes, C.; Plastino, J. Actin dynamics, architecture, and mechanics in cell motility. *Physiol. Rev.* **2014**, *94*, 235–263. [\[CrossRef\]](#) [\[PubMed\]](#)
63. Timm, S.; Nunes-Nesi, A.; Parnik, T.; Morgenthal, K.; Wienkoop, S.; Keerberg, O.; Weckwerth, W.; Kleczkowski, L.A.; Fernie, A.R.; Bauwe, H. A cytosolic pathway for the conversion of hydroxypyruvate to glycerate during photorespiration in Arabidopsis. *Plant Cell* **2008**, *20*, 2848–2859. [\[CrossRef\]](#) [\[PubMed\]](#)
64. Tran, E.J.; King, M.C.; Corbett, A.H. Macromolecular transport between the nucleus and the cytoplasm: Advances in mechanism and emerging links to disease. *Biochim. Biophys. Acta* **2014**, *1843*, 2784–2795. [\[CrossRef\]](#)
65. Kodihla, M.; Stochaj, U. Nuclear transport: A switch for the oxidative stress-signaling circuit? *J. Signal. Transduct.* **2012**, *2012*, 208650. [\[CrossRef\]](#)
66. Dos Santos, A.; Toseland, C.P. Regulation of Nuclear Mechanics and the Impact on DNA Damage. *Int. J. Mol. Sci.* **2021**, *22*, 3178. [\[CrossRef\]](#)
67. Mimura, T.; Joyce, N.C. Replication competence and senescence in central and peripheral human corneal endothelium. *Investig. Ophthalmol. Vis. Sci.* **2006**, *47*, 1387–1396. [\[CrossRef\]](#)
68. Sheerin, A.N.; Smith, S.K.; Jennert-Burston, K.; Brook, A.J.; Allen, M.C.; Ibrahim, B.; Jones, D.; Wallis, C.; Engelmann, K.; Rhys-Williams, W.; et al. Characterization of cellular senescence mechanisms in human corneal endothelial cells. *Aging Cell* **2012**, *11*, 234–240. [\[CrossRef\]](#)
69. Senturk, S.; Mumcuoglu, M.; Gursoy-Yuzugullu, O.; Cingoz, B.; Akcali, K.C.; Ozturk, M. Transforming growth factor-beta induces senescence in hepatocellular carcinoma cells and inhibits tumor growth. *Hepatology* **2010**, *52*, 966–974. [\[CrossRef\]](#)
70. Li, Z.Y.; Chen, Z.L.; Zhang, T.; Wei, C.; Shi, W.Y. TGF-beta and NF-kappaB signaling pathway crosstalk potentiates corneal epithelial senescence through an RNA stress response. *Aging* **2016**, *8*, 2337–2354. [\[CrossRef\]](#)
71. Salminen, A.; Kauppinen, A.; Kaarniranta, K. Emerging role of NF-kappaB signaling in the induction of senescence-associated secretory phenotype (SASP). *Cell. Signal.* **2012**, *24*, 835–845. [\[CrossRef\]](#)
72. Liu, R.M.; Desai, L.P. Reciprocal regulation of TGF-beta and reactive oxygen species: A perverse cycle for fibrosis. *Redox Biol.* **2015**, *6*, 565–577. [\[CrossRef\]](#) [\[PubMed\]](#)
73. Wu, J.; Niu, J.; Li, X.; Wang, X.; Guo, Z.; Zhang, F. TGF-beta1 induces senescence of bone marrow mesenchymal stem cells via increase of mitochondrial ROS production. *BMC Dev. Biol.* **2014**, *14*, 21. [\[CrossRef\]](#) [\[PubMed\]](#)
74. Davalli, P.; Mitic, T.; Caporali, A.; Lauriola, A.; D'Arca, D. ROS, Cell Senescence, and Novel Molecular Mechanisms in Aging and Age-Related Diseases. *Oxid. Med. Cell. Longev.* **2016**, *2016*, 3565127. [\[CrossRef\]](#)
75. Tong, L.; Tergaonkar, V. Rho protein GTPases and their interactions with NFkappaB: Crossroads of inflammation and matrix biology. *Biosci. Rep.* **2014**, *34*, e00115. [\[CrossRef\]](#)
76. Du, F.; Qi, X.; Zhang, A.; Sui, F.; Wang, X.; Proud, C.G.; Lin, C.; Fan, X.; Li, J. MRTF-A-NF-kappaB/p65 axis-mediated PDL1 transcription and expression contributes to immune evasion of non-small-cell lung cancer via TGF-beta. *Exp. Mol. Med.* **2021**, *53*, 1366–1378. [\[CrossRef\]](#) [\[PubMed\]](#)
77. Zorova, L.D.; Popkov, V.A.; Plotnikov, E.Y.; Silachev, D.N.; Pevzner, I.B.; Jankauskas, S.S.; Babenko, V.A.; Zorov, S.D.; Balakireva, A.V.; Juhaszova, M.; et al. Mitochondrial membrane potential. *Anal. Biochem.* **2018**, *552*, 50–59. [\[CrossRef\]](#)
78. Zhdanov, A.V.; Andreev, D.E.; Baranov, P.V.; Papkovsky, D.B. Low energy costs of F1Fo ATP synthase reversal in colon carcinoma cells deficient in mitochondrial complex IV. *Free. Radic. Biol. Med.* **2017**, *106*, 184–195. [\[CrossRef\]](#)

79. Redmann, M.; Darley-USmar, V.; Zhang, J. The Role of Autophagy, Mitophagy and Lysosomal Functions in Modulating Bioenergetics and Survival in the Context of Redox and Proteotoxic Damage: Implications for Neurodegenerative Diseases. *Aging Dis.* **2016**, *7*, 150–162. [\[CrossRef\]](#)
80. Yao, Z.; Klionsky, D.J. An unconventional pathway for mitochondrial protein degradation. *Autophagy* **2016**, *12*, 1971–1972. [\[CrossRef\]](#)
81. Haeussler, S.; Kohler, F.; Witting, M.; Premm, M.F.; Rolland, S.G.; Fischer, C.; Chauve, L.; Casanueva, O.; Conradt, B. Autophagy compensates for defects in mitochondrial dynamics. *PLoS Genet.* **2020**, *16*, e1008638. [\[CrossRef\]](#)
82. Kubli, D.A.; Gustafsson, A.B. Mitochondria and mitophagy: The yin and yang of cell death control. *Circ. Res.* **2012**, *111*, 1208–1221. [\[CrossRef\]](#)
83. Li, X.; Zhang, W.; Cao, Q.; Wang, Z.; Zhao, M.; Xu, L.; Zhuang, Q. Mitochondrial dysfunction in fibrotic diseases. *Cell Death Discov.* **2020**, *6*, 80. [\[CrossRef\]](#)
84. Whelan, K.A.; Chandramouleeswaran, P.M.; Tanaka, K.; Natsuzaka, M.; Guha, M.; Srinivasan, S.; Darling, D.S.; Kita, Y.; Natsugoe, S.; Winkler, J.D.; et al. Autophagy supports generation of cells with high CD44 expression via modulation of oxidative stress and Parkin-mediated mitochondrial clearance. *Oncogene* **2017**, *36*, 4843–4858. [\[CrossRef\]](#) [\[PubMed\]](#)
85. Zhao, X.; Wang, Y.; Wang, Y.; Li, S.; Chen, P. Oxidative stress and premature senescence in corneal endothelium following penetrating keratoplasty in an animal model. *BMC Ophthalmol.* **2016**, *16*, 16. [\[CrossRef\]](#) [\[PubMed\]](#)
86. Jiang, G.J.; You, X.G.; Fan, T.J. Ultraviolet B irradiation induces senescence of human corneal endothelial cells in vitro by DNA damage response and oxidative stress. *J. Photochem. Photobiol. B Biol.* **2022**, *235*, 112568. [\[CrossRef\]](#)
87. Park, W.H. The effects of exogenous H<sub>2</sub>O<sub>2</sub> on cell death, reactive oxygen species and glutathione levels in calf pulmonary artery and human umbilical vein endothelial cells. *Int. J. Mol. Med.* **2013**, *31*, 471–476. [\[CrossRef\]](#) [\[PubMed\]](#)
88. Zorov, D.B.; Juhaszova, M.; Sollott, S.J. Mitochondrial reactive oxygen species (ROS) and ROS-induced ROS release. *Physiol. Rev.* **2014**, *94*, 909–950. [\[CrossRef\]](#) [\[PubMed\]](#)
89. Snezhkina, A.V.; Kudryavtseva, A.V.; Kardymon, O.L.; Savvateeva, M.V.; Melnikova, N.V.; Krasnov, G.S.; Dmitriev, A.A. ROS Generation and Antioxidant Defense Systems in Normal and Malignant Cells. *Oxidative Med. Cell. Longev.* **2019**, *2019*, 6175804. [\[CrossRef\]](#)
90. Desale, S.E.; Chidambaram, H.; Chinnathambi, S. G-protein coupled receptor, PI3K and Rho signaling pathways regulate the cascades of Tau and amyloid-beta in Alzheimer's disease. *Mol. Biomed.* **2021**, *2*, 17. [\[CrossRef\]](#)
91. Jiang, F.; Xu, X.R.; Li, W.M.; Xia, K.; Wang, L.F.; Yang, X.C. Monotropein alleviates H<sub>2</sub>O<sub>2</sub> induced inflammation, oxidative stress and apoptosis via NFκB/AP1 signaling. *Mol. Med. Rep.* **2020**, *22*, 4828–4836. [\[CrossRef\]](#)
92. da Silva, P.F.L.; Ogrodnik, M.; Kucheryavenko, O.; Glibert, J.; Miwa, S.; Cameron, K.; Ishaq, A.; Saretzki, G.; Nagaraja-Grellscheid, S.; Nelson, G.; et al. The bystander effect contributes to the accumulation of senescent cells in vivo. *Aging Cell* **2019**, *18*, e12848. [\[CrossRef\]](#) [\[PubMed\]](#)
93. Yun, H.R.; Jo, Y.H.; Kim, J.; Shin, Y.; Kim, S.S.; Choi, T.G. Roles of Autophagy in Oxidative Stress. *Int. J. Mol. Sci.* **2020**, *21*, 3289. [\[CrossRef\]](#) [\[PubMed\]](#)
94. Moskal, N.; Riccio, V.; Bashkurov, M.; Taddese, R.; Datti, A.; Lewis, P.N.; Angus McQuibban, G. ROCK inhibitors upregulate the neuroprotective Parkin-mediated mitophagy pathway. *Nat. Commun.* **2020**, *11*, 88. [\[CrossRef\]](#)
95. Weber, A.J.; Herskowitz, J.H. Perspectives on ROCK2 as a Therapeutic Target for Alzheimer's Disease. *Front. Cell. Neurosci.* **2021**, *15*, 636017. [\[CrossRef\]](#)

**Disclaimer/Publisher's Note:** The statements, opinions and data contained in all publications are solely those of the individual author(s) and contributor(s) and not of MDPI and/or the editor(s). MDPI and/or the editor(s) disclaim responsibility for any injury to people or property resulting from any ideas, methods, instructions or products referred to in the content.